Research paper

Fabrication of covalently linked graphene-mediated [FeFe]-hydrogenases biomimetic photocatalytic hydrogen evolution system in aqueous solution

Rui-Xia Li[a,1], Xiang-Ting Ren[a,1], Ming-Yi Tang[c,*], Ming-Xi Chen[a], Guan-Bo Huang[a], Chang-Hui Fang[c], Ting Liu[a], Zhan-Heng Feng[d], Yi-Bing Yin[a], Ya-Mei Guo[a], Shun-Kang Mei[a], Jing Yan[a,b,*]

[a] Department of Chemistry, School of Science, Tianjin University, Tianjin 300072, China
[b] Collaborative Innovation Center of Chemical Science and Engineering (Tianjin), Tianjin 300072, China
[c] Department of Applied Chemistry, School of Science, Tianjin University of Commerce, Tianjin 3001341, China
[d] National Demonstration Center for Experimental Chemistry Education, Nankai University, Tianjin 300071, China

ARTICLE INFO

ABSTRACT

Two novel complexes $[Fe_2(\mu\text{-}SC_3H_6S)(CO)_5][Fc(PPh_2)CHO]$ (**3**) and 5-{$[Fe_2(\mu\text{-}SC_3H_6S)(CO)_5](PPh_2Fc)$}-10, 15, 20-triphenylporphyrin (**4**), which contain ferrocene-based ligand to simulate the role of the active site of [FeFe]-hydrogenases (H-Cluster), are synthesized and characterized successfully. A graphene-mediated [FeFe]-hydrogenases biomimetic nanohybrid (TPP-NHCO-GO-[3Fe2S]) **6** is fabricated by linking organic photosensitizer tetraphenylporphyrin (TPP) and complex **3** to graphene oxide (GO) via the covalent bond. The new nanohybrid **6** is characterized by elemental analysis, Fourier transform infrared spectroscopy (FTIR), transmission electron microscopy (TEM) and inductively coupled plasma atomic emission spectrometry (ICP-AES). By comparing the ultraviolet-visible (UV-vis) absorption, fluorescence emission and time-resolved fluorescence, it can be found the efficiency of electron transfer has been obviously improved with the presence of GO, and the efficiency of electron transfer in intramolecular system is higher than that in intermolecular system. These results are also supported by the photo-induced H_2 production experiments with corresponding catalytic systems in water. Besides, the cystine is used as the sacrificial electron donor for light catalytic reaction in aqueous solution, which improves the efficiency of photocatalytic H_2 production compared with the common electron donors, such as ascorbic acid (H_2A), triethanolamine (TEOA), glucose or $Na_2S_2O_3$.

1. Introduction

Photo-induced H_2 production is a promising approach to direct conversion of solar energy into storable hydrogen fuel that has been regarded as a green energy carrier [1,2]. Thanks to the diligent exploration of biological scientists, some kinds of enzymes called "Hydrogenases" which can catalyze the interconversion of H_2 with protons in a wide variety of microorganisms have been discovered [3,4]. Hydrogenases are normally classified into two major families in literature based on the metal content of their respective binuclear catalytic centers, namely [NiFe]-hydrogenases and [FeFe]-hydrogenases, respectively [5,6]. Both of them can catalyze in production and consumption of H_2, and the [FeFe]-hydrogenases present more rapid reaction rate for H_2 production [7]. Therefore, mimicking the reactivity of [FeFe]-hydrogenases by active-site models is more focused on biomimetic studies

currently [8–13], especially in light-driven H_2 production [14–18], since this kind of biomimetic catalysts rely on inexpensive first-row transition metals and may overcome the difficulties on extraction and preservation of natural enzymes to some extent. However, in comparison to the natural enzymes, the poor electron transfer efficiency of [FeFe]-hydrogenases models limits the H_2 production catalyzed by the bionic photocatalytic systems [19,20]. Additionally, since most of the [FeFe]-hydrogenases models are organometallic compounds, their photocatalytic or electrocatalytic experiments are usually carried out in organic solution [21–23]. Therefore, improvements along these two directions are required to achieve the efficient "green chemistry" circle between H_2O and H_2 for more perspective applications.

For the past few years, graphene has been found as a single-atom-thick planar sheet of sp^2-bonded carbon atoms regularly arranged in a honeycomb lattice [24,25]. The excellent electronic properties of this
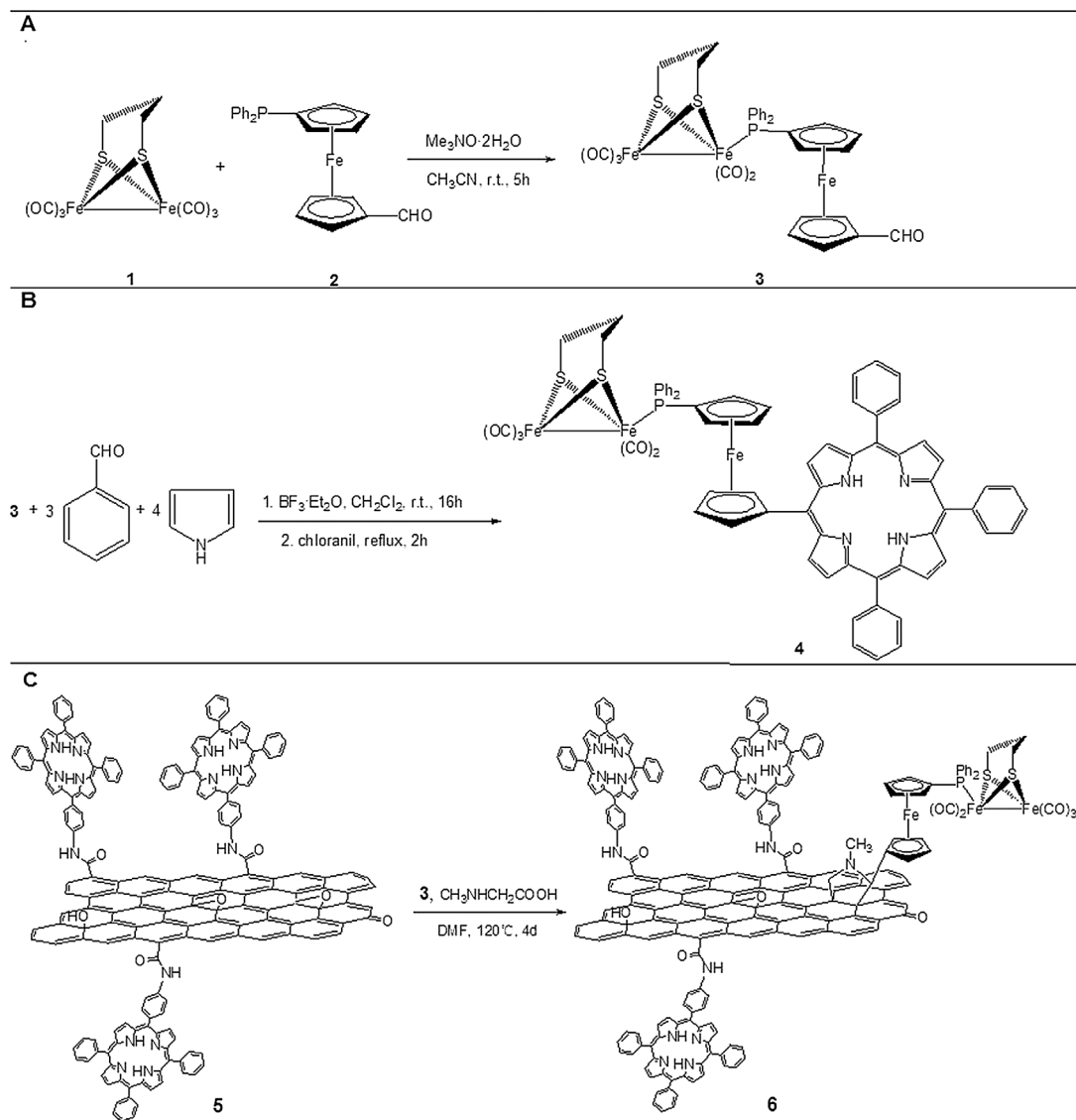

Scheme 1. The synthesis routes of **3** (A), **4** (B) and **6** (C).

exciting functional material have been well documented recently [26]. Graphene oxide (GO), a derivative of graphene, has also been widely studied across many disciplines, including photocatalytic, high-frequency electronics, and energy storage or conversion, due to its easily-reached large size as well as its extraordinary physicochemical and structural properties [27]. Benefiting from its large surface area and the plentiful oxygen-containing groups on its surface, such as epoxy ($-C-O-C-$) groups, carboxylic ($-COOH$), and hydroxyl ($-OH$), GO can be well dispersed in water and provides a few reactive sites for the chemical modification of classical methods [28,29].

Taking advantage of the outstanding properties of GO in electron transfer and water solubility, as shown in Scheme 1, we designed and synthesized a graphene-mediated [FeFe]-hydrogenases biomimetic nanohybrid (TPP-NHCO-GO-[3Fe2S], **6**) to frame a photocatalytic system in aqueous solution, which composed of active site analogue of [FeFe]-hydrogenases ([Fe$_2$(μ-SC$_3$H$_6$S)(CO)$_5$][Fc(PPh$_2$)CHO], complex **3**), optoelectronic active porphyrin molecules (tetraphenylporphyrin, TPP), GO nanosheet and electronic sacrificial agents. The TPP functionalized GO nanocomposite (TPP-NHCO-GO, **5**) was synthesized via an amide bond using an amine-functionalized tetraphenylporphyrin (5-4(amino-phenyl)-10, 15, 20-triphenyl porphyrin, TPP-NH$_2$ for short) and GO in N,N-dimethylformamide (DMF) according to the literature method

[30]. The main reasons for choosing porphyrin-type photosensitizer are: 1) many porphyrins are naturally occurring such as haem, and most of them have photochemical electron-transfer ability prospectively and low or no negative environmental impact; 2) porphyrin macrocycles are conjugated systems which have intense absorption bands in the visible region typically; 3) TPP can absorb as much as 46% of the energy of sunlight, and the efficiency of energy conversion of dye-sensitized solar cell has been increased to 13% by using the modified TPP lately [31–33].

The ferrocene group-containing triiron-propanedithiolate complex **3**, which can be regarded as the active site model of [FeFe]-hydrogenases, has been successfully synthesized and linked to the surface of GO via covalent bond by Prato reaction (a straightforward approach for functionalizing a single-walled carbon cube or C$_{60}$ to assure the photo-induced electron transfer between the different moieties) [34–37]. According to crystallographic [38,39] and FTIR spectroscopic [40] studies, the active site of [FeFe]-hydrogenases, so-called H-cluster [41], can be viewed as a cubic [4Fe4S] cluster linked by a protein backbone bridging cysteinyl sulfur ligand to a butterfly [2Fe2S] cluster, as shown in Scheme 2A. Rauchfuss and co-workers reported the suitably modified ferrocenes can replicate the behaviors of the [4Fe4S] clusters without their complications due to the chemical inertness and the mild redox

A

X = NH, CH$_2$, O
The natural [FeFe]-hydrogenases

B
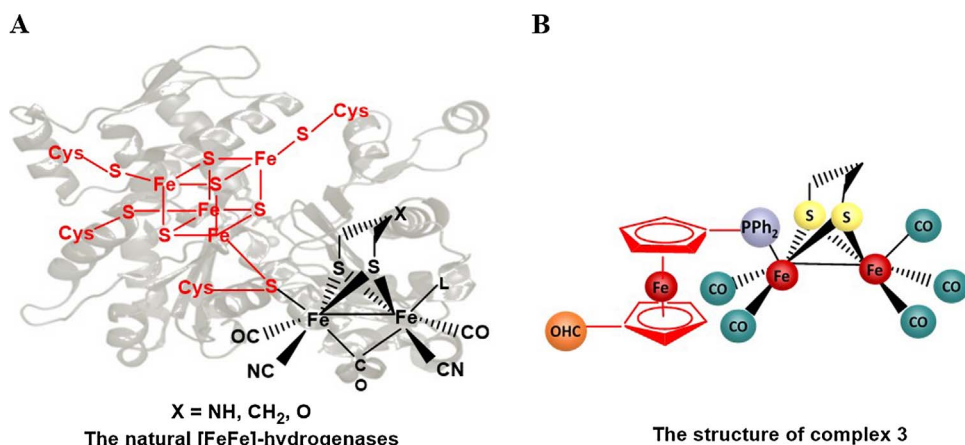
The structure of complex 3

potential of the ferrocene-derived ligand [42]. They also suggested the mechanism for hydrogen evolution reaction (HER) by their biomimetic [FeFe]-Hydrogenase models included the electron transfer procedure from the ferrocenylphosphine ligand covalently attached to the FeFe core, which could work as a redox-active ligand with sufficient diving force to simulate the critical role of the appended [4Fe4S] cluster in catalysis [43]. Thus, the phosphine ligand 1′-(diphenylphosphino)-1-ferrocenecarboxaldehyde (**2**) was designed to substitute CO ligand of parent complex Fe$_2(\mu$-SC$_3$H$_6$S)(CO)$_6$ (**1**) to mimic the electron-transfer role of [4Fe4S] cluster to some extent (Scheme 2B).

In addition, utilizing the aldehyde group on ferrocene, as shown in Scheme 1B, complex **3** reacted with benzaldehyde and pyrrole in "one-pot" to synthesize a new complex (5-{[Fe$_2(\mu$-SC$_3$H$_6$S)(CO)$_5$](PPh$_2$Fc)}-10, 15, 20-triphenylporphyrin, **4**), which has a porphyrin-like photo-sensitizing group and can realize light-induced intramolecular electron transfer process as expected (be verified by fluorescence emission in the following).

Besides, it's worth pointing out that we chose cystine as the electron donor for the photo-induced H$_2$ production in the water based on the inspiration from the protein surrounding of complicated metallo-thioether ligand Cys-SFe$_4$S$_4$(SCys)$_3$ in the H-cluster (Scheme 3). Compared with the catalytic systems with common electron donors, such as

ascorbic acid (H$_2$A), triethanolamine (TEOA), glucose or Na$_2$S$_2$O$_3$, the efficiency of H$_2$ production had been improved by several times due to the participation of cystine. Fluorescence emission, time-resolved fluorescence and gas chromatography (GC) etc. were used to compare the efficiency of electron transfer through different processes (intramolecular or intermolecular) and the photo-induced H$_2$ production in aqueous solution with diverse catalytic systems. The results prove the role of GO on hydrophilicity and support the assumption that higher electron transfer ability may lead to better efficiency of photo-induced H$_2$ production from [FeFe]-hydrogenases mimic system in water, which will probably expand our horizon in the biomimetic area.

2. Experimental section

2.1. Materials

Dichloromethane (CH$_2$Cl$_2$), DMF, chloroform (CHCl$_3$) and acetonitrile (MeCN) were distilled respectively from CaH$_2$ under N$_2$, and tetrahydrofuran (THF) from Na/benzophenone ketyl. Pyrrole was freshly distilled and ferrocene was recrystallized by hexane before use. H$_2$A, TEOA, Na$_2$S$_2$O$_3$, LiEt$_3$BH, Ph$_2$PCl, BF$_3 \cdot$Et$_2$O, CH$_3$NHCH$_2$COOH, acetic acid (HOAc), glucose, cystine, benzaldehyde, chloranil, petroleum

Cystine =

Graphene-mediated [FeFe]-hydrogenases biomimetic catalytic system for visible-light-induced H$_2$ production in aqueous solution
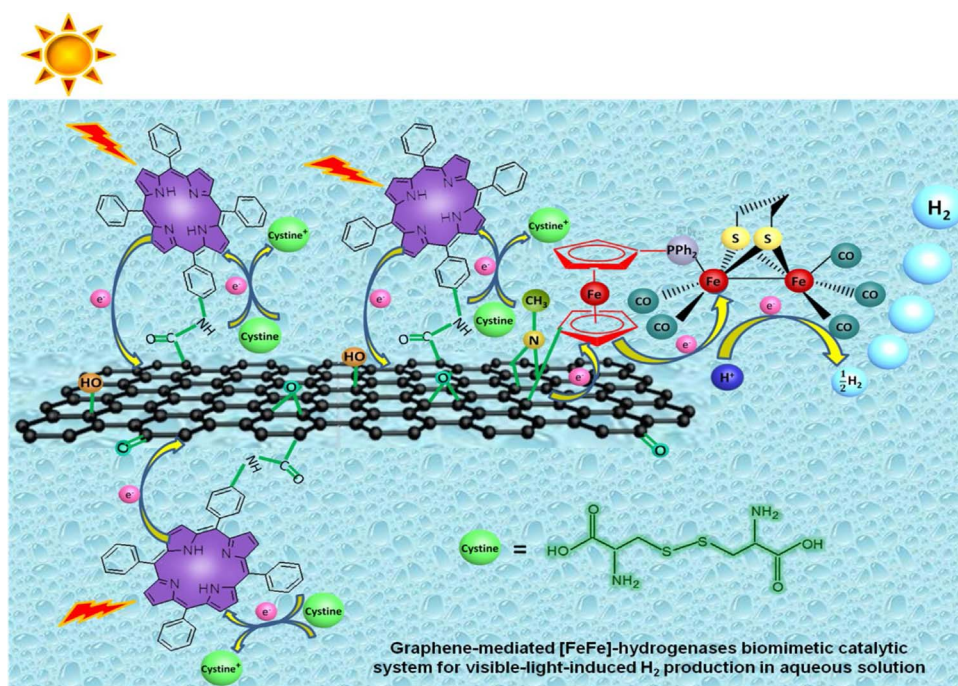
ether, methanol and alumina paste were available commercially and used as received. **1** [44], **2** [45], Me$_3$NO·2H$_2$O [46], **5** [30], TPP [47] and tetrabutylammonium hexafluorophosphate (*n*-Bu$_4$NPF$_6$) [48] were prepared according to literature procedures, respectively. Besides, large-scale and water-soluble GO was prepared by the modified Hummers method [49].

2.2. Instruments and methods

The UV–vis spectral measurements were carried out with a Shimadzu UV-3600 spectrophotometer. The steady-state fluorescence was measured by using F-97 fluorospectrophotometer. FTIR were recorded on a Thermo Scientific Nicolet AVATAR 360 infrared spectrophotometer. NMR were recorded on a Bruker Avance 400 MHz spectrometer. Elemental analyses were performed on Germany Elementar Vario EL analyzer. Melting points were determined on X-6 apparatus (Tektronix). Time-resolved fluorescence was performed on a Fluorolog3 instrument (Japan, HORIBA JOBIN YVON) with excitation at 419 nm. The amount of Fe element of **6** was determined by ICP-AES spectroscopy (ICP-VISTA-MPX, USA VARIAN). TEM measurements were performed using a Philips Tecnai G2F20 microscope at 200 kV. Electrochemical measurements were made using a CHI 660D electrochemical station. Hydrogen production experiments were carried out in a photocatalytic reactor (USA ACE GLASS). The produced photoproduct of H$_2$ was characterized by GC analysis (CP 3800 Varian) using nitrogen as the carrier gas with a TDX-01 column and a thermal conductivity detector. A single crystal of **3** suitable for X-ray diffraction analyses was grown by slow evaporation of the CHCl$_3$ solution at room temperature, a single crystal of **3** was mounted on a Rigaku XtaLAB mini diffractometer. Data were collected at 294(2) K by using a graphite crystal monochromator situated in the incident beam with Mo Kα radiation (λ = 0.71073 Å) in the ω-2θ scanning mode. Empirical absorption corrections were applied using REQAB and the program CrystalClear was used for integration of the diffraction profiles [50]. The structures were solved by direct methods using SHELXS of the SHELXTL package and refined with SHELXL [51]. Hydrogen atoms were located using the geometric method. CCDC 1493452 contains the supplementary crystallographic data for this paper. These data can be obtained free from the Cambridge Crystallographic Data Centre via www.ccdc.cam.ac.uk/data_request/cif.

2.3. Electrochemical experiments

Electrochemical measurements were made using the electrochemical station at a scan rate of 0.1 V s^{-1}. All the voltammograms were obtained in a three-electrode cell with a glassy carbon working electrode (diameter: 3 mm), a Pt wire counter electrode, and an Ag/Ag$^+$ (0.01 M AgNO$_3$/0.1 M *n*-Bu$_4$NPF$_6$ in CH$_3$CN) reference electrode under N$_2$ atmosphere. A solution of 0.1 M *n*-Bu$_4$NPF$_6$ in CH$_3$CN was used as electrolyte in cyclic voltammetric experiments. The working electrode was polished with 0.02–0.05 μm alumina paste and sonicated in water before use. Ferrocene was added as an internal reference and all potentials are quoted against this ferrocene/ferrocenium (Fc/Fc$^+$) potential.

2.4. Hydrogen production experiments

Electron donors were dissolved in water to make an aqueous solution at a certain concentration (1.8 × 10^{-3} M). The pH values of the solution were adjusted by sodium hydroxide solution or hydrochloric acid, and were determined by a pH meter. Then certain amounts of catalyst and electron donor were taken to mix in a quartz tube. The volume of the sample solution for photocatalytic H$_2$ production was 5.0 mL. Before irradiation, the sample and the reactor were saturated with nitrogen gas to eliminate oxygen. Then the reactor was sealed with an airtight cap. The solution kept on swirling by a magneton during the

photocatalytic process. An Hg lamp (450 W) with a cutoff filter (λ > 380 nm) was used as light source. The produced H$_2$ was characterized by GC analysis. And the H$_2$/N$_2$ (1.0 mL, 0.477 v%) was injected as the external standard for quantitative GC-TCD analysis. After irradiation, the H$_2$ evolved was measured and calculated by comparing with the integral area between 1.0 mL sample in the quartz tube and the external standard.

2.5. Synthesis and characterization of 3, 4 and 6

All reactions were carried out under an atmosphere of highly purified nitrogen by using standard Schlenk technique. The synthesis routes of **3**, **4** and **6** were shown in Scheme 1.

2.5.1. Synthesis and characterization of 3

Me$_3$NO·2H$_2$O (55.6 mg, 0.5 mmol) was added to the 20.0 mL MeCN solution of **1** (193.0 mg, 0.5 mmol). The mixture was stirred at room temperature for 15 min before **2** (199.0 mg, 0.5 mmol) was added. The new mixture was stirred for 5 h at room temperature. The solvents was removed at reduced pressure and the residue was subjected to TLC separation by THF/hexane (1:3, V/V). Collecting the second red band got 230.0 mg (60.8%) of **3** as a red brown solid, m.p. 52 − 53 °C. The data of NMR and elemental analysis for **3** were shown in the Supporting Information.

2.5.2. Synthesis and characterization of 4

The mixture of **3** (529.3 mg, 0.7 mmol), PhCHO (0.2 mL, 2.1 mmol), pyrrole (0.2 mL, 2.8 mmol), and BF$_3$·OEt$_2$ (3.6 × 10^{-2} mL, 0.3 mmol) in CH$_2$Cl$_2$ (200.0 mL) was stirred in the dark at room temperature for 16 h to give a brown-red solution. After adding chloranil (689.0 mg, 2.8 mmol), the mixture was refluxed for 2 h. Then solvent was removed under reduced pressure and the residue was subjected to TLC by CH$_2$Cl$_2$/petroleum ether (1:1, V/V). From the second green band, complex **4** was obtained as a purple-red solid (152.0 mg, 17.2%), m.p. 231 °C (dec.). The data of NMR and elemental analysis for **4** were shown in the Supporting Information.

2.5.3. Synthesis and characterization of 6

160.0 mg of **5** was added into 300.0 mL DMF. After sonicating for about 1 h, the dispersed suspension of **5** was added **3** (33.3 mg, 4.4 × 10^{-2} mmol) and CH$_3$NHCH$_2$COOH (35.6 mg, 0.4 mmol), then the mixture was heated to 120 °C. The same amount of **3** and CH$_3$NHCH$_2$COOH were added again at intervals of 24 h and 48 h successively. The reaction mixture was heated for 4 days in total. When it was cooled to the room temperature, the solution was filtered through a nylon membrane filter (0.22 μm) and then the filter cake was washed thoroughly with THF and methanol. The residue was repeatedly sonicated and filtered until all the unreacted ingredients were washed away. The final sample was then dried under vacuum at room temperature and used for further characterization by UV-vis, FTIR, fluorescence and TEM studies.

3. Results and discussion

3.1. X-ray crystal structures of 3

The structure of **3** was studied with X-ray crystallography. The ORTEP view of **3** was shown in Fig. 1. Details of crystal data and structure refinements were summarized in Table S1 and selected bond distances and angles were presented in Table S2. The main part of **3** is a butterfly [2Fe2S] cluster which links to the ferrocenecarbaldehyde through diphenyl phosphorus ligand. The Fe(1)-Fe(2) bond distance [2.5174(9) Å] is slightly shorter than those of [FeFe]-hydrogenases [2.55–2.62 Å] [36,37]. The P(1)-C(21) bond distance and Fe(2)-P(1) bond distance are [1.813(2) Å] and [2.2468(10) Å] respectively, showing the difference between the covalent bond and coordinate
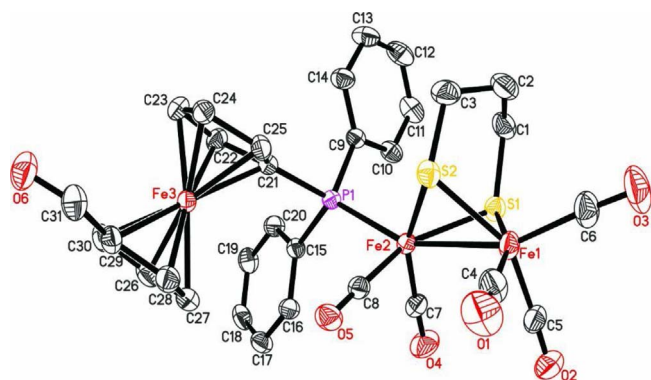
Fig. 1. ORTEP plot of **3** with 30% probability level ellipsoids.

bond. The bond angle of C(6)-Fe(1)-Fe(2) [153.36(11) °] and P(1)-Fe(2)-Fe(1) [155.30(3) °] are almost similar, which suggests that C(6) and P(1) are both located on the top spot of the tetragonal pyramid of Fe(1) and Fe(2).

3.2. FTIR analysis

The FTIR of **3**, **4**, **5**, **6** and GO were shown in Fig. 2. Owing to the effect of diphenyl phosphorus ligand, the peaks at $2041\,cm^{-1}$, $1975\,cm^{-1}$ and $1914\,cm^{-1}$, which are characteristic of the C≡O stretch of the terminal carbonylic groups on the [2Fe2S] cluster of **3**, shift significantly to lower wavenumbers than complex **1** (the peaks at $2072\,cm^{-1}$, $2033\,cm^{-1}$ and $1993\,cm^{-1}$ as reported in the literature) [52]. The C=O stretch of the aldehyde group of **3** emerges at $1683\,cm^{-1}$. However, the FTIR of **4** shows the C≡O stretch of the terminal carbonylic groups on the [2Fe2S] cluster emerges at $2048\,cm^{-1}$, $1977\,cm^{-1}$ and $1952\,cm^{-1}$. The results are also significantly lower than the corresponding peaks of **1**, but slightly higher than **3**. The peak at $1683\,cm^{-1}$ disappears, suggesting the formation of covalent bond and the successful synthesis of **4**. Besides, the peak at $1720\,cm^{-1}$ is characteristic of the C=O stretch of the carboxylic group on the GO [30]. For **5** and **6**, new broad bands emerge at $1642\,cm^{-1}$ and $1645\,cm^{-1}$ respectively, which accord with the C=O characteristic stretching band of the amide group [53]. It is a pity the C≡O stretching peaks of the terminal carbonylic groups on the [2Fe2S] cluster of **6** have no obvious signals, presumably because of the low concentration or the instrumental sensitivity limit.

3.3. The TEM images of GO, 5 and 6

The TEM images of GO, **5** and **6** were displayed in Fig. 3. The TEM
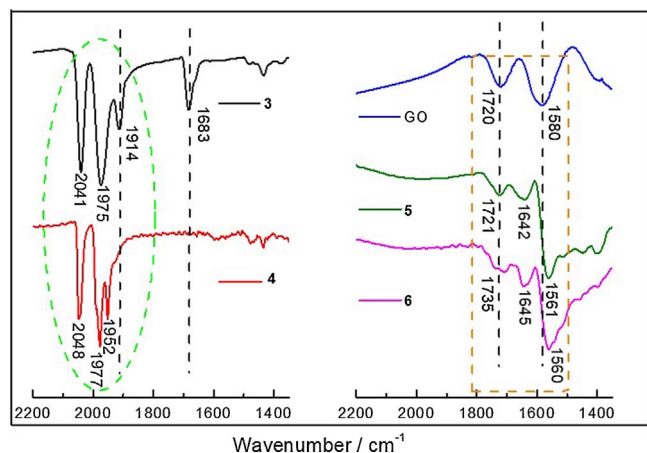

Fig. 2. FTIR of **3**, **4**, GO, **5** and **6**.

image of GO (Fig. 3A) shows the typical wrinkle morphology and thin layers of GO, which is consistent with the literature [54]. In the image of **5** (Fig. 3B), the edge of GO is significantly roughened by the coverage of soft material. The results suggest the presence of TPP-NH_2 attached to the GO edge [30]. As shown in Fig. 3C, the irregular surface of GO in the image of **6** suggests the complex **3** was linked to **5** successfully. The TEM-EDX analysis of **6** had been measured (Fig. S1). The presence of Fe, S and P also confirmed the structure of **6** as we expected. Besides, the content ratio of [3Fe2S] cluster of **6** was determined by Fe, while the content of Fe was measured by the inductively coupled plasma atomic emission spectrometry (ICP-AES). We also measured the content of N in **5** and **6** through elemental analysis. Finally, by calculation of the results of ICP-AES and elemental analysis above, we got the contents of TPP and [3Fe2S] moiety are $2.9 \times 10^{-7}\,mol \cdot mg^{-1}$ and $6.0 \times 10^{-7}\,mol \cdot mg^{-1}$ respectively for **6**, and the content of TPP is $4.4 \times 10^{-7}\,mol \cdot mg^{-1}$ for **5**. The detailed calculations were shown in Supporting Information.

3.4. Electrochemistry of 2, 3 and 4

Cyclic voltammetry studies of **2**, **3** and **4** were performed in a CH_3CN solution with 0.1 M n-Bu_4NPF_6 as the supporting electrolyte to examine the redox properties of them. As shown in Fig. S2, the cyclic voltammogram for **2** displays an irreversible reduction peak at -2.49 V vs Fc/Fc$^+$. When HOAc was added, the initial reduction peak anodally shifted to about -2.34 V (2 mM) and the current intensity arose with adding of the acid. These are consistent with the description about the aldehyde groups in previous literature [55]. Therefore, the reduction peak of **2** at -2.49 V can be assigned to the getting electron process of the aldehyde groups.

An uncomplicated redox at $E_{1/2} = 0.64$ V (the half-wave potential) of **3** is assigned to the reversible Fe^{II}/Fe^{III} oxidation of the ferrocene moiety (Fig. 4), which is close to the reported value in the literature about the ferrocene-based compound [56]. There is an irreversible reduction peak of **3** at $E_{pc} = -1.83$ V, which is assigned to [Fe^IFe^I] + e$^-$ → [Fe^IFe^0] [57,58]. In addition, the cyclic voltammogram for **3** displays another irreversible reduction peak at -2.51 V. The electrochemical behavior of catalytic proton reduction by **3** was researched in the presence of HOAc. When HOAc was added, the peak of **3** at -1.83 V increases slightly and stops to grow with sequential addition of HOAc. However, a new reduction peak about -2.12 V appeared and the current intensity had a linear correlation about the added HOAc concentration (as shown in inset), which suggests an electrochemical catalysis happened [57–59]. With adding of HOAc, the reduction peak at -2.51 V of **3** made anodic shift to about -2.35 V (2 mM) and the current intensity rose. Since the similar potential shift with **2**, this peak can be assigned to the reduction of the aldehyde group [55]. Besides, the stability of the ferrocene moiety under acidic condition shows that, as a redox-active ligand used to simulate the role of the [4Fe4S] cluster, the ferrocene-derived ligand of **3** shows chemical inertness, so the HER reaction could be localized at the [2Fe2S] core. The ECEC (Electrochemical-Chemical-Electrochemical-Chemical) mechanism can account for the electrochemical behavior of **3** [60,61]. In this catalytic cycle, **3** is reduced at -1.83 V by getting one electron and then is monoprotonated, forming **3H**. **3H** is reduced at -2.12 V to form **3H$^-$** and then **3H$^-$** earns another proton to give off molecular H_2 and regenerate **3** to complete the catalytic cycle.

The cyclic voltammogram of **4** was shown in Fig. S3. The reversible redox peak at -0.36 V of **4** is assigned to the redox of ferrocene. Compared with **3**, this peak has a significant negative shift due to the absence of the electron withdrawing effect of the aldehyde group [62]. Two quasi-reversible redox peaks are observed at -1.18 V and -1.53 V, which are assigned to the reversible redox of tetraphenylporphyrin-like moiety. Besides, the irreversible reduction peaks of **4** at -1.90 V and -2.30 V can be assigned to [Fe^IFe^I] + e$^-$ → [Fe^IFe^0] and [Fe^IFe^0] + e$^-$ → [Fe^0Fe^0], respectively [57,58]. The
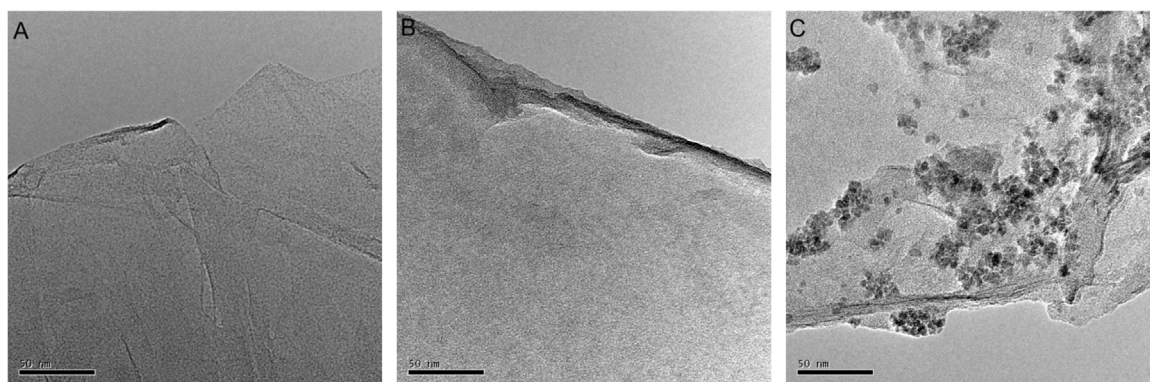
Fig. 3. The TEM (bar scale 50 nm) images of GO (A), **5** (B) and **6** (C).
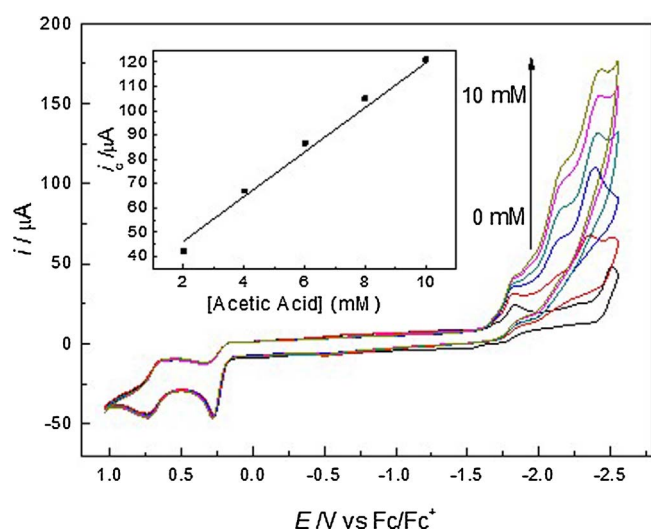
Fig. 4. Cyclic voltammogram of **3** (1.0 mM) with HOAc (0–10 mM) in 0.1 M n-Bu$_4$NPF$_6$/CH$_3$CN at a scan rate of 0.1 V · s^{-1} (Inset: current intensity versus HOAc concentration).

electrochemical behavior of catalytic proton reduction of **4** was also studied in the presence of HOAc. As shown in Fig. S4, the redox of ferrocene moiety in **4** had no influence with sequential addition of HOAc, which suggest that ferrocene moiety didn't catalyze proton reduction. The two reversible redox peaks of tetraphenylporphyrin-like moiety turned irreversible and moved more positively due to protonation of the porphyrin group probably. The irreversible reduction peak of **4** at −1.90 V increased slightly but not grew steadily with sequential addition of HOAc. However, the peak of **4** at −2.30 V grew remarkably with adding the acid and the current intensity had a linear correlation about the added HOAc concentration (as shown in inset). Unlike **3**, another EECC (Electrochemical-Electrochemical-Chemical-Chemical) mechanism is probably working for proton catalysis of **4** based on the gathered experimental evidence [58]. The first step of the possible catalytic process of **4** is being reduced at −1.90 V, followed by getting another electron at −2.30 V to produce **4**$^{2-}$. Protonation make **4**$^{2-}$ gain two protons successively to produce H$_2$, thereby accomplishing the catalytic cycle.

3.5. Light-driven H$_2$ evolution

Light-driven H$_2$ evolution catalyzed by **3**, **4** or **6** were studied in aqueous solution using a mercury lamp (450 W) with a cutoff filter (λ > 380 nm). The photocatalytic activity of **6** was investigated by varying the electron donors from H$_2$A, TEOA, glucose, Na$_2$S$_2$O$_3$, to cystine. As shown in Fig. 5A, the amounts of H$_2$ were significantly different with various electron donors. The most H$_2$ evolution was

achieved when cystine was used as an electron donor. We hypothesized the reasons for it are: 1) disulfide could probably regenerate to be the active relay species through the possible intermetdiate-thiyl radical [63]; 2) the structural characteristic of amino acid is more conducive to providing a proton channel for the catalytic system, which can simulate the protein environment to some extent, and then reproduce the key role of essential proton pathway for H$_2$ production of the natural [FeFe]-hydrogenase via hydrogen bonding utilizing water wires or residue side chains [64,65].

The pH value also influenced the H$_2$ production. Decreasing or increasing the acidity of the solution resulted in the amounts of H$_2$ evolution dropping dramatically (Table S3). The maximum amount of photocatalytic H$_2$ evolution was achieved at pH = 1.0. We speculated the reasons for it are that both the reduction potential of the proton in the solution and the electron donating ability of cystine are pH value dependent. As the acidity increases, the reduction potential of the proton make positive shift, which results in increasing of the hydrogen evolution rate [66]. However, cystine will be protonated at extremely low pH value, leading to weakening the electron donating ability of lone pair of electrons and hampering the proton transport channel in the catalytic system to some extent [67]. Therefore, light-driven H$_2$ evolution should occur at an optimized acidic condition.

The control experiments were performed, and the results were shown in Fig. 5B. The efficiency of H$_2$ production was obviously reduced or even disappeared in absence of **3**, **5**, cystine or irradiation. These results show that [3Fe2S] moiety (catalyst), photosensitizer groups, electron donor and irradiation are all essential for H$_2$ evolution of this photocatalytic system.

The stability and recyclability of **6** were examined by the repeated experiments. For each repeated photocatalytic experiment, the nanohybrid **6** was reused after washed adequately by centrifugation. The H$_2$ evolution remained as much as 86.5% of the initial value after the third cycle (Fig. 6A). In addition, we can also measure the content of [3Fe2S] moiety of **6** remained 81.7% after the third repeated photocatalytic experiment by calculating the results of ICP-AES.

To identify the efficiency of electron transfer within different systems, we compared the photocatalytic H$_2$ production performance of four systems under the same experimental conditions. As shown in Fig. 6B, the light-driven H$_2$ evolution displayed a ranking of System A > System D > System B > System C. The results suggested that: 1) the photocatalytic H$_2$ production efficiencies of intramolecular electron transfer systems are higher than those of intermolecular systems; 2) the H$_2$ production efficiencies of the catalyst systems with GO-mediated are higher than those of the catalyst systems without GO. In addition, the amounts of H$_2$ evolved of System A are several times more than those of other systems in aqueous solution. These support the key role of GO on hydrophilicity and confirmed our initial assumption that increasing the electron transferring ability could result in promoting the efficiency of photo-induced H$_2$ production in the water to a certain extent.
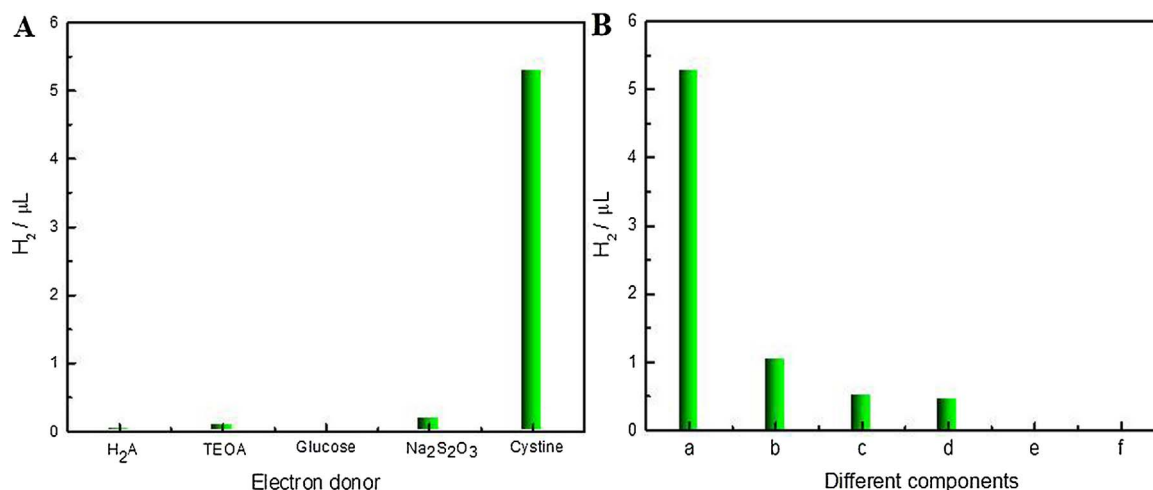
Fig. 5. The amounts of photocatalytic H$_2$ evolution over **6** with different electron donors in water (A); the amounts of photocatalytic H$_2$ evolution for the control experiments (B) (The detailed experimental conditions were elaborated in the Supporting Information.).

3.6. The photophysical properties of 3, 4 and 6

The photophysical properties of **3**, **4** and **6** were studied to understand the electron transfer. Considering the similarity of the porphyrin ring group, we used TPP as a reference in the following analysis and discussion hereinafter. The UV–vis absorption of **4** displayed a strong Soret absorption at 422 nm and Q-bands at 509 nm, 576 nm and 666 nm, which were similar to the reported UV–vis absorption of TPP (Fig. 7A) and H$_2$FcPh$_3$P [FcPh$_3$P = 5-ferrocenyl-10, 15, 20-triphenyl porphyrin(2⁻)] [68]. The results explain there is a weak interaction between the photosensitizer porphyrin ring and the [3Fe2S] moiety at the ground state.

Fig. 7B shows the UV–vis absorption of **3**, **5** and **6**. In the spectrum of **6**, a peak of [3Fe2S] moiety appeared at the similar position and a Soret absorption at 418 nm only blue shifted by 2 nm compared with **5** (420 nm). The results suggest that **3** had been successfully linked to nanocomposite **5** via a covalent bond, and the conjugate structure of the nanohybrid had not been broken seriously by Prato reaction.

The fluorescence of the different complexes, nanohybrids and the associated mixtures were shown in Fig. 8A. Each of the complexes or nanohybrids had two emission peaks. The emission peaks of **4** (651 nm, 715 nm), **5** (651 nm, 712 nm) and **6** (651 nm, 713 nm) were quenched by 68.4%, 80.6% and 84.9%, upon TPP (650 nm, 713 nm) respectively, which probably caused by the electron transfer of intramolecular [69].

Since the spectroscopic overlaps between the emission of TPP (the peak at 650 nm and 713 nm) and the absorption of both [3Fe2S] moiety (about 357 nm) and GO (mostly below 600 nm) were limited (Fig. S5), the energy transfer from the excited photosensitive group to [3Fe2S] moiety or GO is negligible [70]. Also, **6** showed 52.2% more quenching of the fluorescence emission than **4**, which can be probably attributed to the important role of mediation by GO [71]. The emission peaks of the equimolar mixture of TPP and **3** were quenched by 25.5% upon TPP, while the emission peaks of **4** were quenched by 68.4% upon TPP. Similarly, the quenching efficiency of the equimolar mixture of **5** and **3** (81.0%) is less than that of **6** (84.9%). These results probably suggest the efficiency of electron transfer in intramolecular system is higher than that in intermolecular system.

The fluorescence lifetime of TPP moiety in **4**, **5** and **6** displayed dual exponential fluorescence decay. The shorter lifetime items can be assigned to the photo-induced electron transfer from TPP to the accepter moiety of each substance, while the longer items are from the fluorescence of unquenched TPP [72]. **4**, **5** and **6** were measured in DMF (Fig. 8B) and the results were summarized in Table 1. The rate constant of the electron transfer (k_{ET}) of **4** was calculated using Eq. (1) [72,73]:

$$k_{ET} = 1/\tau_f - 1/\tau_0 \text{ (1)}$$

in which τ_f and τ_0 are the fluorescence lifetimes of **4** and TPP respectively. The k_{ET} of **5** and **6** were calculated following the same method
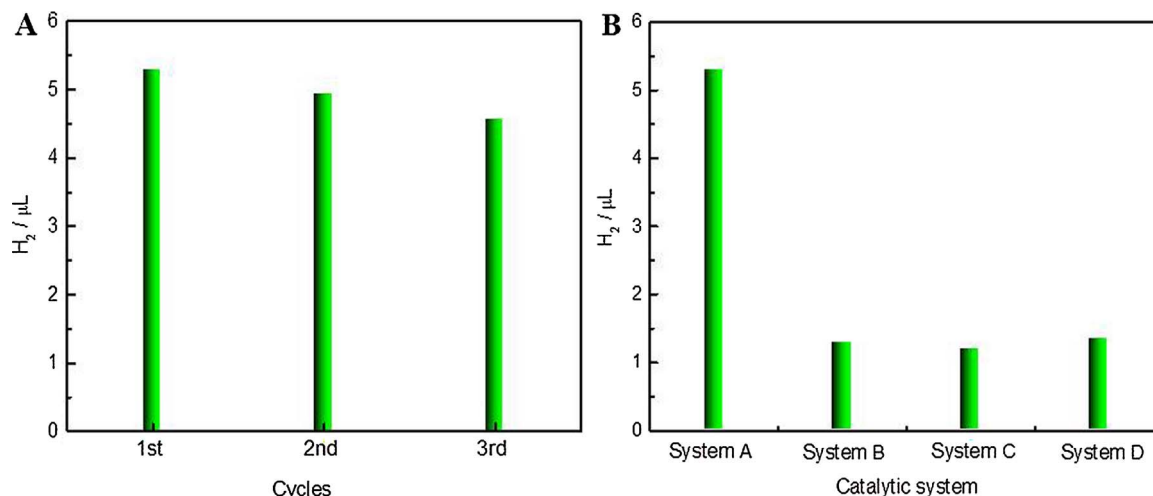

Fig. 6. The photocatalytic H$_2$ evolution of **6** for recycling (A); photocatalytic H$_2$ production of the catalytic systems with different catalysts in the cysteine aqueous solution (B) (System A: **6**; System B: **4**; System C: **3** + TPP; System D: **3** + **5**; the detailed experimental conditions were elaborated in the Supporting Information.).
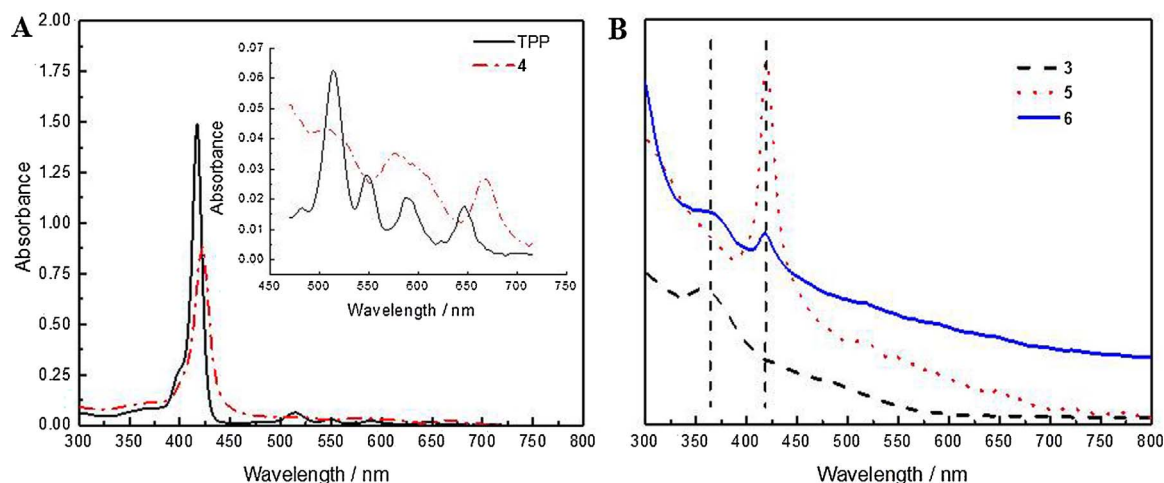
Fig. 7. UV–vis absorption of TPP (3.0×10^{-6} M) and **4** (3.0×10^{-6} M) in CH_2Cl_2 (A); comparison of the UV–vis absorption peak position of **3**, **5** and **6** in DMF (B).

and the results were also listed in Table 1. As shown in Table 1, the electron transfer rates satisfy a ranking of $k_{ET}^{6} > k_{ET}^{4}$, which probably suggests the intramolecular electron transfer between the photosensitive group and the [3Fe2S] moiety has been promoted by GO, which is consistent with the result of the fluorescence quenching observation above.

3.7. Comparing and analyzing the suggested electron transfer processes of different photocatalytic H_2 production systems

Referring to the electrochemical data above, we analyzed the free-energy changing for the electron transfer (ΔG_{ET}) of **4**, **5** and **6**. (The details are shown in Supporting Information. All redox potentials extracted from electrochemical measurements and modified by Fc/Fc$^+$, are displayed in Table 2. We assumed TPP as the donor and [3Fe2S] moiety as the accepter within the electron transfer procedure of **4**. The first (E_{0-01}) and second (E_{0-02}) singlet excited energy of TPP are 1.92 eV and 2.98 eV respectively. The potential for one-electron oxidation E_{ox} of TPP is at 0.76 V, and the potential for one-electron reduction E_{red} of **4** is at -1.90 V. The resulted ΔG_{ET1} and ΔG_{ET2} of **4** were 0.74 eV and -0.32 eV respectively. These suggest the electron transfer from the second singlet excited of the donor to the acceptor is exothermic. These results were similar to the models of hydrogenases which realized intramolecular electron transfer [22,33,74]. The ΔG_{ET} of **5** and **6** are estimated following a similar method and the results are listed in

Table 1
Fluorescence properties of TPP, **4**, **5** and **6** (excited at 419 nm in DMF).

	TPP	4	5	6
τ_1 (ns)		4.55	3.85	3.67
τ_2 (ns)	10.41	10.05	9.77	9.35
k_{ET} ($\times 10^8$ s^{-1})	-	1.24	1.64	1.76

Table 2
ΔG_{ET} for **4**, **5** and **6**.

	E_{0-01}(eV) (the first singlet excited state)	E_{0-02}(eV) (the second singlet excited state)	E(ox) (V)	E(red) (V)	ΔG_{ET1}(eV) (the first singlet excited state)	ΔG_{ET2}(eV) (the second singlet excited state)
4	1.92 (TPP)	2.98 (TPP)	0.76 (TPP)	-1.90 (**4**)	0.74	-0.32
5	1.92 (TPP)	2.98 (TPP)	0.76 (TPP)	-1.17 (GO)	0.01	-1.05
6	1.92 (**5**)	2.96 (**5**)	0.98 (**5**)	-1.83 (**3**)	0.89	-0.15
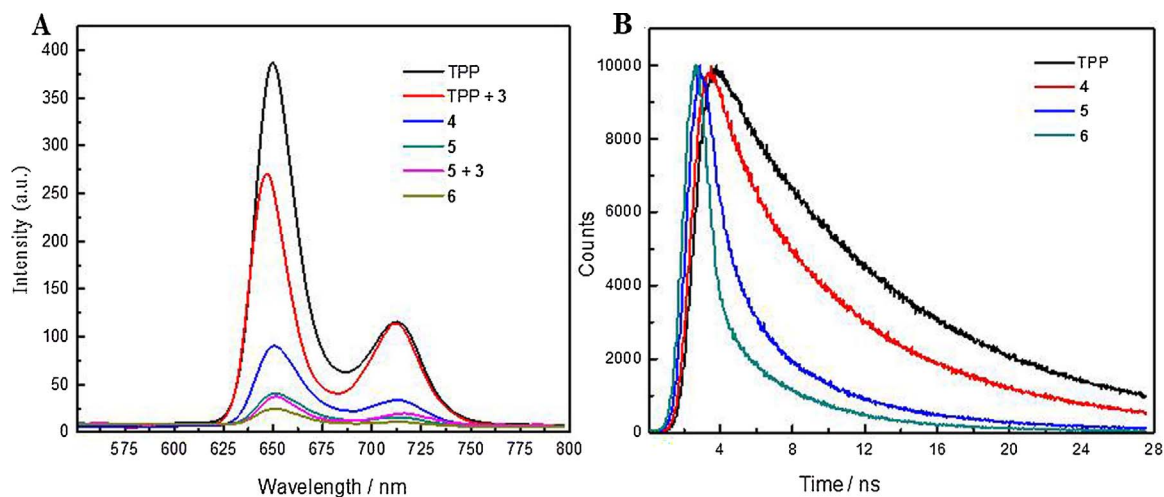
Fig. 8. Fluorescence of TPP, the mixture of TPP and **3** (TPP + **3**), the mixture of **5** and **3** (**5** + **3**), **4**, **5** and **6** in DMF with the normalization (the absorbance of the Soret band excitation wavelength (419 nm) to the same value (0.024)) (A); fluorescence decay lifetime of TPP, **4**, **5** and **6** in DMF with excitation at 419 nm (B).
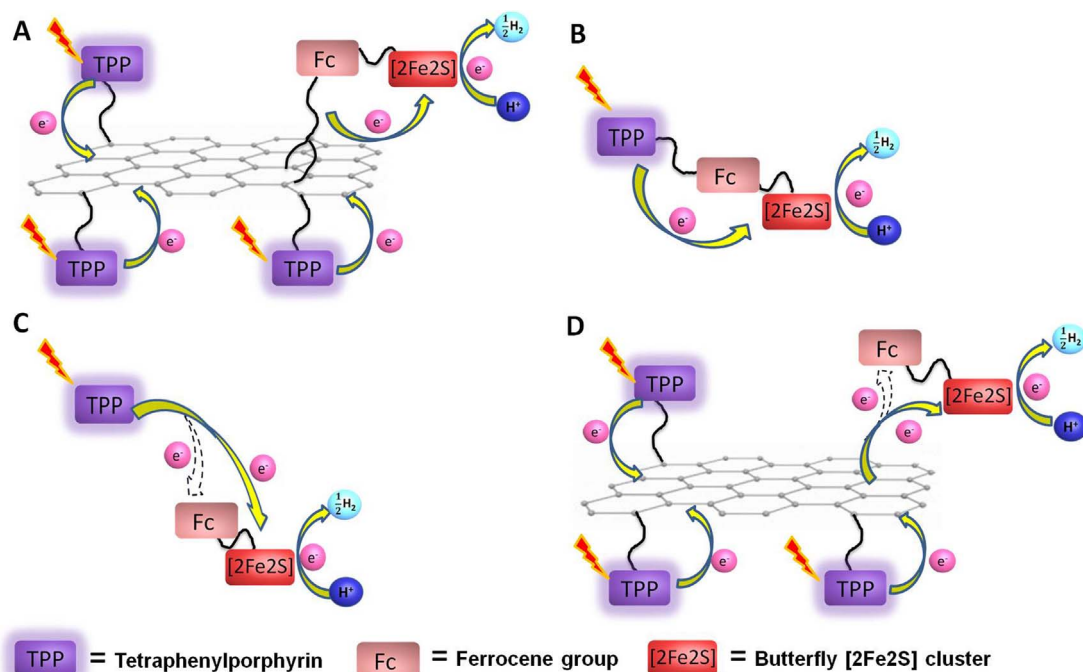
Fig. 9. Suggested processes of electron transfer within **6** (A), **4** (B), the mixture of **3** and TPP (C) and the mixture of **3** and **5** (D).

Table 2. As shown in Table 2, the data of **5** suggest the electron transfer from the second singlet excited of the donor to the acceptor is also exothermic, which is in keeping with the previous report on the photocurrent and optical properties of GO with porphyrin [71,75,76]. As for **6**, we assumed TPP-NH-GO (**5**) moiety as the donor and the [3Fe2S] moiety as the accepter within the electron transfer procedure. Then the ΔG_{ET2} of **6** was -0.15 eV. According to the results of the calculation above, it could be speculated the photo-induced electron from TPP may spontaneously transfer to [3Fe2S] moiety in the nanohybrid **6** via GO.

The suggested schematic diagrams of electron transferring within different complexes or nanohybrids were described in Fig. 9. Also, the comparative analysis diagrams of the corresponding processes were shown in Fig. 10. All the data which are used in Fig. 10 are shown in Table S4. By comparing and analyzing the diagrams and corresponding experimental data above, we could easily find that: 1) the first electron transfer processes from the excited states of photosensitive groups to the [3Fe2S] moieties are all thermodynamically feasible in each catalytic system, so the efficiencies of the hydrogen production are probably
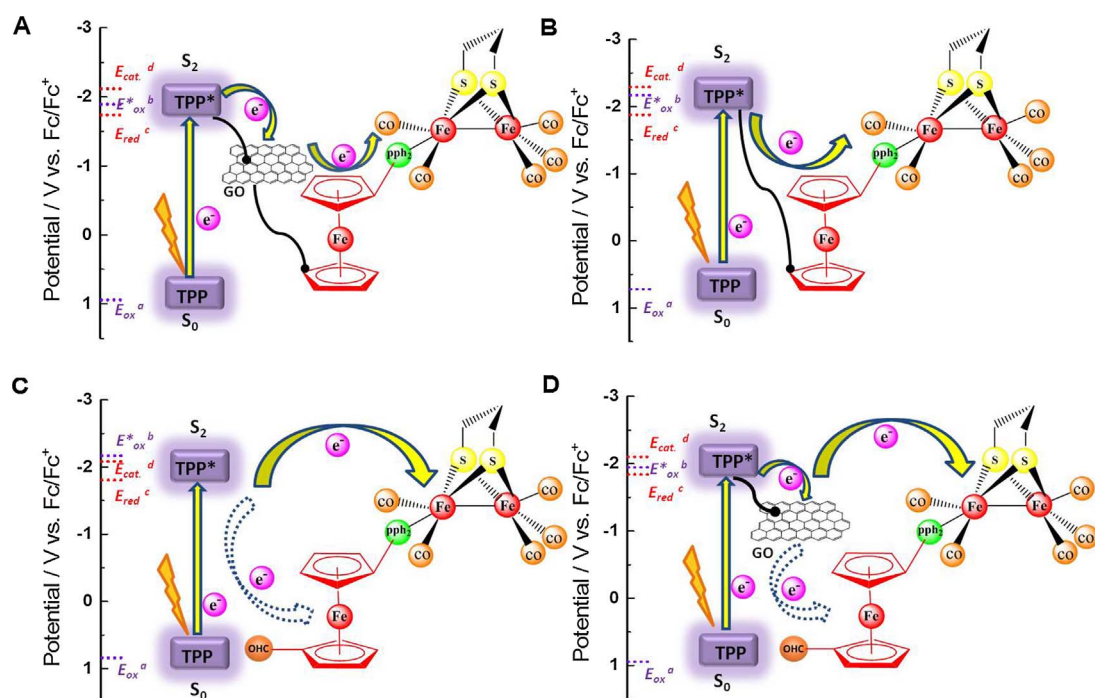

Fig. 10. The comparative analysis of electron transfer processes for **6** (A), **4** (B), the mixture of **3** and TPP (C) and the mixture of **3** and **5** (D) (E_{ox}^a: the oxidation potential of the ground state of TPP moiety; $E^*_{ox}{}^b$: the oxidation potential of the excited state of TPP moiety; E_{red}^c: the reduction potential of Fe^{I}Fe^I/Fe^{I}Fe^0 in each systems; E_{cat}^d: the reduction potential of catalyzing H$_2$ production by obtaining the second electron in each system).

more dependent on the paths of the electron transfer; 2) although the intermolecular electron transfer systems (System C and System D) have more possible paths than the intramolecular electron transfer systems (System A and System B), the oxidizing substance in the aqueous solution or the groups easy to be reduced are more likely to consume some of the electrons, which probably lead to the lower efficiencies of electron transfer than those in the intramolecular systems linked by covalent bond directly; 3) in contrast to the catalytic systems without GO participation (System B and System C), the GO mediated systems (System A and System D) can provide the "electron highway" for electron transfer between the photosensitive group to the catalyst, and the GO's conjugate structure and high electrical conductivity are more favorable for forming of charge separation and more conductive to the electron transfer [71]. Besides, by comparing the System B and System D, the characteristics of GO's hydrophily and large surface area are more helpful to increase the dispersion of the organic compounds attached on GO in water, which leads to the intermolecular electron transfer system (System D) producing slightly more hydrogen than the intramolecular one (System B).

According to the estimated data in Table S4, most of the systems lack enough driving force to support the second electron transfer from the excited TPP to 2Fe site, which might hinder the H_2 production of mimic systems from being as efficient as the natural [FeFe]-hydrogenases. We speculate that if more oxidizing groups on the GO nanosheet are reduced with the premise of preserving the GO's dispersibility in water to a certain extent, the integrity of the conjugated structure will be increased and the loss of the electrons in the transfer will be further decreased. With enhancing the conjugation of the electron transfer channel and the driving force of the excited photosensitizer, the efficiency of the electron transfer and the hydrogen production will be further improved, which is one of the interests for our future efforts and is being currently pursued in our laboratory.

4. Conclusions

In summary, we have successfully synthesized and characterized two [3Fe2S] complexes **3** and **4** as the models of the [FeFe]-hydrogenases. Both **3** and **4** have a ferrocence group to simulate the function of the [4Fe4S] cluster of H-cluster in the natural [FeFe]-hydrogenases enzyme. Besides, a graphene mediated [FeFe]-hydrogenases biomimetic nanohybrid **6** has been designed and synthesized for the first time as far as we know. Benefiting from the outstanding hydrophility and electrical conductivity of GO, the novel nanohybrid has a better dispersion in water and higher efficiency of electron transfer. UV–vis absorption, fluorescence emission and time-resolved fluorescence studies suggest the photocatalytic H_2 production efficiencies of intramolecular electron transfer systems are higher than those of intermolecular systems. Meanwhile, the experimental results show the H_2 production efficiencies of the catalyst systems with GO mediated are higher than those without GO. In addition, we found that cystine can be used as the electron donor which may improve the efficiency of photo-induced H_2 production catalytic system for several times than other commonly used sacrificial agents in aqueous solution. Therefore, we speculate the higher efficiency of the photocatalytic H_2 production is likely to earn by using functional material GO as the media and introducing cystine into the system of light-driven H_2 evolution as the electron donor. All the work may pave the way to promote the efficiency of visible-light-driven H_2 evolution for [FeFe]-hydrogenases bionic system.

Acknowledgments

Appendix A. Supplementary data

Supplementary data associated with this article can be found, in the online version, at http://dx.doi.org/10.1016/j.apcatb.2017.09.062.

References

[1] M. Gratzel, Nature 414 (2001) 338–344.
[2] M.G. Walter, E.L. Warren, J.R. Mckone, S.W. Boettcher, Q.X. Mi, E.A. Santori, N.S. Lewis, Chem. Rev. 110 (2010) 6446–6473.
[3] R. Cammack, Nature 397 (1999) 214–215.
[4] M.W.W. Adams, E.I. Stiefel, Science 282 (1998) 1842–1843.
[5] V. Artero, G. Berggren, M. Atta, G. Caserta, S. Roy, L. Pecqueur, M. Fontecave, Acc. Chem. Res. 48 (2015) 2380–2387.
[6] D. Schilter, J.M. Camara, M.T. Huynh, S. Hammes-Schiffer, T.B. Rauchfuss, Chem. Rev. 116 (2016) 8693–8749.
[7] M. Frey, ChemBioChem 3 (2002) 153–160.
[8] C. Tard, C.J. Pickett, Chem. Rev. 109 (2009) 2245–2274.
[9] L.-C. Song, Acc. Chem. Res. 38 (2005) 21–28.
[10] F. Wen, X. Wang, L. Huang, G. Ma, J. Yang, C. Li, ChemSusChem 5 (2012) 849–853.
[11] N.T. Hunt, J.A. Wright, C. Pickett, Inorg. Chem. 55 (2016) 399–410.
[12] D. Mersch, C.Y. Lee, J.Z. Zhang, K. Brinkert, J.C. Fontecilla-Camps, A.W. Rutherford, E. Reisner, J. Am. Chem. Soc. 137 (2015) 8541–8549.
[13] Y. Honda, H. Hagiwara, S. Ida, T. Ishihara, Angew. Chem. Int. Ed. 55 (2016) 8045–8048.
[14] A.P.S. Samuel, D.T. Co, C.L. Stern, M.R. Wasielewski, J. Am. Chem. Soc. 132 (2010) 8813–8815.
[15] L.-Z. Wu, B. Chen, Z.-J. Li, C.-H. Tung, Acc. Chem. Res. 47 (2014) 2177–2185.
[16] T. Yu, Y. Zeng, J. Chen, Y.-Y. Li, G. Yang, Y. Li, Angew. Chem. Int. Ed. 52 (2013) 5631–5635.
[17] A. Adamska-Venkatesh, S. Roy, J.F. Siebel, T.R. Simmons, M. Fontecave, E. Artero, W. Reijerse Lubitz, J. Am. Chem. Soc. 137 (2015) 12744–12747.
[18] Y. Li, T.B. Rauchfuss, Chem. Rev. 116 (2016) 7043–7077.
[19] M. Wang, L. Sun, ChemSusChem 3 (2010) 551–554.
[20] R. Lomoth, S. Ott, Dalton Trans. (2009) 9952–9959.
[21] L. Beaume, M. Clé mancey, G. Blondin, C. Greco, F.Y. Pétillon, P. Schollhammer, J. Talarmin, Organometallics 33 (2014) 6290–6293.
[22] L.-C. Song, M.-Y. Tang, S.-Z. Mei, J.-H. Huang, Q.-M. Hu, Organometallics 26 (2007) 1575–1577.
[23] L.-C. Song, J. Yan, Y.-L. Li, D.-F. Wang, Q.-M. Hu, Inorg. Chem. 48 (2009) 11376–11381.
[24] K.S. Novoselov, A.K. Geim, S.V. Morozov, D. Jiang, M.I. Katsnelson, I.V. Grigorieva, S.V. Dubonos, A.A. Firsov, Nature 438 (2005) 197–200.
[25] K.S. Novoselov, A.K. Geim, S.V. Morozov, D. Jiang, Y. Zhang, S.V. Dubonos, I.V. Grigorieva, A.A. Firsov, Science 306 (2004) 666–669.
[26] J.N. Coleman, Acc. Chem. Res. 46 (2013) 14–22.
[27] V. Georgakilas, J.N. Tiwari, K.C. Kemp, J.A. Perman, A.B. Bourlinos, K.S. Kim, R. Zboril, Chem. Rev. 116 (2016) 5464–5519.
[28] I.V. Lightcap, P.V. Kamat, Acc. Chem. Res. 46 (2013) 2235–2243.
[29] D. Wei, B. Wu, Y. Guo, G. Yu, Y. Liu, Acc. Chem. Res. 46 (2013) 106–115.
[30] Y. Xu, Z. Liu, X. Zhang, Y. Wang, J. Tian, Y. Huang, Y. Ma, X. Zhang, Y. Chen, Adv. Mater. 21 (2009) 1275–1279.
[31] I. Okura, Coord Chem. Rev. 68 (1985) 53–99.
[32] S. Mathew, A. Yella, P. Gao, R. Humphry-Baker, B.F.E. Curchod, N. Ashari-Astani, I. Tavernelli, U. Rothlisberger, Md.K. Nazeeruddin, M. Grätzel, Nat. Chem. 6 (2014) 242–247.
[33] L.-C. Song, M.-Y. Tang, F.-H. Su, Q.-M. Hu, Angew. Chem. Int. Ed. 45 (2006) 1130–1133.
[34] M.A. Herrero, E. Vazquez, M. Prato, Handbook of Carbon Nano Materials 1 (2011), pp. 271–323.
[35] S.K. Das, A.S.D. Sandanayaka, N.K. Subbaiyan, M. Zandler, O. Ito, F. D'Souza, Chem. Eur. J. 18 (2012) 11388–11398.
[36] B. Ballesteros, G. d. l. Torre, C. Ehli, G.M. Aminur Rahman, F. Agullo-Rueda, D.M. Guldi, T. Torres, J. Am. Chem. Soc. 129 (2007) 5061–5068.
[37] F. Caporossi, B. Floris, P. Galloni, E. Gatto, M. Venanzi, Eur. J. Org. Chem. 19 (2006) 4362–4366.
[38] Y. Nicolet, C. Piras, P. Legrand, C.E. Hatchikian, J.C. Fontecilla-Camps, Structure 7 (1999) 13–23.
[39] J.W. Peters, W.N. Lanzilatta, B.J. Lemon, L.C. Seefeldt, Science 282 (1998) 1853–1858.
[40] B.J. Lemon, J.W. Peters, Biochemistry 38 (1999) 12969–12973.
[41] M.W.W. Adams, Biochim. Biophys. Acta. 1020 (1990) 115–145.
[42] J.M. Camara, T.B. Rauchfuss, Nat. Chem. 4 (2012) 26–30.
[43] J.C. Lansing, J.M. Camara, D.E. Gray, T.B. Rauchfuss, Organometallics 33 (2014) 5897–5906.
[44] D. Seyferth, G.B. Womack, M.K. Gallagher, Organometallics 6 (1987) 283–294.
[45] M.E. Wright, Organometallics 9 (1990) 853–856.
[46] J.A. Soderquist, C.L. Anderson, Tetrahedron Lett. 27 (1986) 3961–3962.
[47] A.D. Adler, F.R. Longo, J.D. Finarelli, J. Goldmacher, J. Assour, L. Korsakoff, J. Org. Chem. 32 (1967) 476.
[48] D. Chouffai, G. Zampella, J.-F. Capon, L.D. Gioia, A.L. Goff, F.Y. Pétillon,

P. Schollhammer, J. Talarmin, Organometallics 31 (2012) 1082–1091.

[49] Z. Liu, Q. Liu, Y. Huang, Y. Ma, S. Yin, X. Zhang, W. Sun, Y. Chen, Adv. Mater. 20 (2008) 3924–3930.

[50] Crystal Clear for CCD System Instruction Manual, Rigaku. Corporation, Tokyo Japan, 2009.

[51] G.M. Sheldrick, SHELXTL NT version 5.1, Program for Solution and Refinement of Crystal Structures, University of Göttingen, Germany, 1997, 2017.

[52] E.J. Lyon, I.P. Georgakaki, J.H. Reibenspies, M.Y. Darensbourg, Angew. Chem. Int. Ed. 38 (1999) 3178–3180.

[53] S. Niyogi, E. Bekyarova, M.E. Itkis, J.L. McWilliams, M.A. Hamon, R.C. Haddon, J. Am. Chem. Soc. 128 (2006) 7720–7721.

[54] D.A. Dikin, S. Stankovich, E.J. Zimney, R.D. Piner, G.H.B. Dommett, G. Evmenenko, S.T. Nguyen, R.S. Ruoff, Nature 448 (2007) 457–460.

[55] W.-G.W. Si, C.-H. Tung, L.-Z. Wu, Inorg. Chem. 47 (2008) 8101–8111.

[56] X.D. Hatten, E. Bothe, K. Merz, I. Huc, N. Metzler-Nolte, Eur. J. Inorg. Chem. (2008) 4530–4537.

[57] P. Li, M. Wang, C.-J. He, G.-H. Li, X.-Y. Liu, C.-N. Chen, B. Åkermark, L.-C. Sun, Eur. J. Inorg. Chem. (2005) 2506–2513.

[58] D. Chong, I.P. Georgakaki, R. Mejia-Rodriguez, J. Sanabria-Chinchilla, M.P. Soriaga, M.Y. Darensbourg, Dalton Trans. (2003) 4158–4163.

[59] L.-C. Song, C.-G. Li, J.-H. Ge, Z.-Y. Yang, H.-T. Wang, J. Zhang, Q.-M. Hu, J. Inorg. Biochem 102 (2008) 1973–1979.

[60] I.K. Pandey, S.M. Mobin, N. Deibel, B. Sarkar, S. Kaur-Ghumaan, Eur. J. Inorg. Chem (2015) 2875–2882.

[61] A.K. Vannucci, S. Wang, G.S. Nichol, D.L. Lichtenberger, D.H. Evans, R.S. Glass, Dalton Trans. 39 (2010) 3050–3056.

[62] M. Buda, A. Ion, J.-C. Moutet, E. Saint-Aman, R. Ziessel, J. Electroanal. Chem. 469 (1999) 132–138.

[63] L.-M. Zhao, Q.-Y. Meng, X.-B. Fan, C. Ye, X.-B. Li, B. Chen, V. Ramamurthy, C.-H. Tung, L.-Z. Wu, Angew. Chem. Int. Ed. 56 (2017) 3020–3024.

[64] B. Ginovska-Pangovska, M.-H. Ho, J.C. Linehan, Y. Cheng, M. Dupuis, S. Raugei, W.J. Shaw, Biochim. Biophys. Acta Bioenergy 1837 (2014) 131–138.

[65] A.J. Cornish, B. Ginovska, A. Thelen, J.C.S. da Silva, T.A. Soares, S. Raugei, M. Dupuis, W.J. Shaw, E.L. Hegg, Biochemistry 55 (2016) 3165–3173.

[66] M.S. Zhu, Z. Li, B. Xiao, Y.T. Lu, Y.K. Du, P. Yang, X.M. Wang, ACS Appl. Mater. Interfaces 5 (2013) 1732–1740.

[67] M.S. Zhu, Z. Li, Y.K. Du, Z.G. Mou, P. Yang, ChemCatChem 4 (2012) 112–117.

[68] V.N. Nemykin, G.T. Rohde, C.D. Barrett, R.G. Hadt, J.R. Sabin, G. Reina, P. Galloni, B. Floris, Inorg. Chem. 49 (2010) 7497–7509.

[69] X.-F. Liu, X.-W. Xiao, J. Organomet. Chem. 696 (2011) 2767–2771.

[70] C.-Bo Li, Z.-J. Li, S. Yu, G.-X. Wang, F. Wang, Q.-Y. Meng, B. Chen, K. Feng, C.-H. Tung, L.-Z. Wu, Energy Environ. Sci. 6 (2013) 2597–2602.

[71] M.B.M. Krishna, N. Venkatramaiah, R. Venkatesanb, D.N. Rao, J. Mater. Chem. 22 (2012) 3059–3068.

[72] W. Xu, H.L. Chen, Y.F. Wang, C.T. Zhao, X.Y. Li, S.Q. Wang, Y.X. Weng, ChemPhyChem 9 (2008) 1409–1415.

[73] H. Zhao, C. Chen, Y. Zhu, M. Shi, J. Zheng, J. Nanopart. Res. 14 (2012) 765–772.

[74] P.P. Kumar, G. Premaladha, B.G. Maiya, J. Chem. Sci. 117 (2005) 193–201.

[75] A. Wojcik, P.V. Kamat, ACS Nano 4 (2010) 6697–6706.

[76] A. Wang, W. Yu, Z. Huang, F. Zhou, J. Song, Y. Song, L. Long, M.P. Cifuentes, M.G. Humphrey, L. Zhang, J. Shao, C. Zhang, Sci. Rep. 6 (2016) 23325–23337.